

Rayleigh–Taylor stability criteria for elastic-plastic solid plates and shells

E. L. Ruden^{a)} and D. E. Bell^{b)}

Phillips Laboratory PL/WSQP, Kirtland Air Force Base, New Mexico 87117

(Received 20 December 1996; accepted for publication 25 March 1997)

The Rayleigh–Taylor (R-T) instability theory is usually applied to the acceleration of one fluid by a lower density one, but also becomes applicable to a solid accelerated by a fluid at very high pressure. Approximate analytic R-T stability criteria are derived for both finite and infinitesimal perturbations of the driven surface of an incompressible solid plate of a given thickness, shear modulus, and von Mises yield stress uniformly accelerated by a massless fluid. The Prandtl-Reuss equations of elastic-plastic flow are assumed for the solid. A single degree of freedom, amplitude q , is assumed for the *spatial* dependence of the perturbation, which is approximated to be that of the semi-infinite half-plane ideal fluid linear R-T eigenfunction. The *temporal* dependence of q , however, is determined self-consistently from global energy balance, following a previously published model. The (significant) effect of the *unperturbed* solid's stress tensor is included and related to the converging/diverging geometries of imploding/exploding cylindrical and spherical solid shells for which the model may be applied locally. Correlations with Phillips Laboratory's quasispherical electromagnetic implosions of solid shells are presented. © 1997 American Institute of Physics. [S0021-8979(97)03513-5]

I. INTRODUCTION

Solid matter accelerated by a lower density fluid may exhibit unstable plastic flow at a sufficiently high driving fluid pressure. A number of related analytic^{15,11,22,14} and numerical¹⁷ models have been developed for the acceleration instability of a solid flat plate driven by a lower density fluid, and the effect has been observed quantitatively.^{1,2}

This paper is primarily motivated by the need to quantify instability processes radiographically observed in experiments at Phillips Laboratory USAF (PL) with strongly accelerated solid metal shells, although other applications may be found for the theoretical results presented in devices such as magnetocumulative flux compression current generators and hypervelocity projectiles. PL's 1300 μF , 120 kV (rated) Shiva Star capacitor bank has been used to implode cylindrical and conical aluminum liners by axial current discharge for various applications.^{3–5} More recently, 6061-T6 aluminum liners with an outer-spherical surface have been imploded between conical electrodes.⁶ These liners are designed to preserve their spherical shape to first order (in the thin-shell limit) during the implosion by being machined with a shell thickness proportional to the square of the shells' outer *cylindrical* radius. This balances the liners' areal density with the axial drive current's external magnetic pressure, resulting in a nominally uniform *spherical* radial acceleration.

Figure 1 illustrates an overlay of the inner and outer surfaces inferred from a published radiograph⁶ of one such implosion with the results of a two-dimensional numerical simulation using the Steinburg–Cochran–Guinan dynamical solid properties treatment^{7,8} of program CALE^{9,10} (C-language Arbitrary Lagrangian Eulerian). It is apparent from the radiographic data that an outer perturbation grows during the im-

plosion. One thing that will be shown based on the stability criteria derived in this article is that this observed instability is likely due to the initial machining error of 130 μm .

The principal model developed in this paper is one introduced by White¹¹ that assumes the perturbation has the same spatial distribution as the linear semi-infinite inviscid fluid Rayleigh–Taylor¹² eigenfunction. However, instead of the amplitude growing exponentially, it is determined assuming global energy conservation based on the Prandtl–Reuss equations of elastic-plastic flow.¹³ The material yield strength, shear modulus, and any background stress in the unperturbed plate due to lateral convergence or divergence are taken into account. A parametric relationship between the maximum stable initial perturbation amplitude and the driver pressure, in addition to an ultimate driver pressure beyond which even an infinitesimal perturbation is unstable, are derived. Since references are provided for a more complete introduction to the model developed, details are provided in Sec. II only insofar as is necessary to provide continuity with Sec. III. Derivations of the stability criteria in Sec. III are heuristic in part as they appeal to parameter space dimension spanning graphical representations. Proof of the conditional applicability of the analytic model to magnetically driven solids is provided in Appendix A.

II. INSTABILITY MODEL OF THE SOLID PHASE

Adopting much of the notation of Robinson and Swegle,¹⁴ the analytic plastic flow models cited above are based on either the Prandtl–Reuss (P-R),

$$\dot{\mathbf{S}} + \mathbf{A}\mathbf{S} = 2G\mathbf{D}, \quad (1)$$

or Levy–Mises (L-M),

$$\mathbf{S} = \sqrt{2} s_1 \mathbf{D} / \sqrt{\mathbf{D} \cdot \mathbf{D}}, \quad (2)$$

equations¹³ for elastic-plastic or rigid plastic flow, respectively. Here, over-dot means the time derivative, G is the

^{a)}Electronic mail: ruden@plk.af.mil

^{b)}Present address: U.S. Air Force Academy, HQ USAF/DFP, 2354 Fairchild Dr., Suite 2A8C, USAFA, CO 80840.

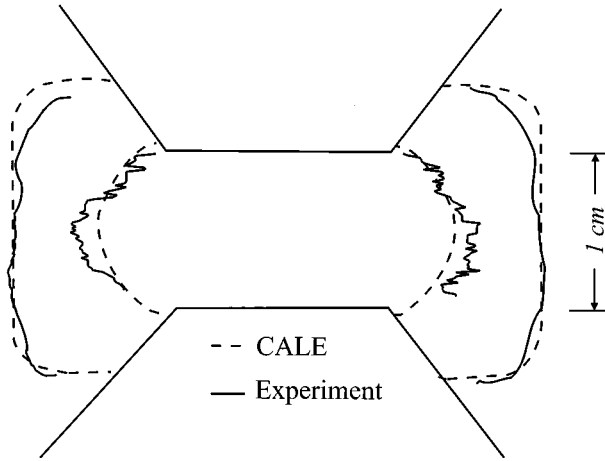


FIG. 1. Simulated and experimental boundary overlay for the quasispherical liner at 14 μ s from start of current. The outer-experimental contour results from a numerical edge detection algorithm from a digitized radiograph. The inner contour is the peak radiograph film density vs cylindrical radius for each z position. This corresponds to the shell's inner-radius contour, assuming uniform shell density (a reasonable approximation according to the simulation).

elastic shear modulus, s_1 is the von Mises yield strength in pure shear, \mathbf{S} is the deviatoric stress tensor ($\mathbf{S} \cdot \mathbf{I} = 0$),

$$\mathbf{D} = \frac{1}{2} (\nabla \mathbf{v} + \nabla \mathbf{v}^T), \quad (3)$$

is the strain rate tensor, with \mathbf{v} being the flow velocity, and

$$\Lambda = \begin{cases} G\dot{W}/s_1^2 & \text{if } J_2 = 2s_1^2 \text{ and } \dot{W} > 0; \\ 0 & \text{if } J_2 < 2s_1^2 \text{ or } \dot{W} < 0. \end{cases} \quad (4)$$

$J_2 = \mathbf{S} \cdot \mathbf{S}$ is self-consistently bounded by $2s_1^2$ in both models (von Mises yield condition), and equals this bound for $\mathbf{D} \neq \mathbf{0}$ in the L-M model. $\dot{W} = \mathbf{S} \cdot \mathbf{D}$ is the noncompressive elastic-plastic work rate density. The cited models are of a perturbed flat plate in the x - z plane of density ρ and unperturbed thickness h driven by a massless fluid of pressure p_0 on the lower y side in a reference frame linearly accelerating in the unit vector $\hat{\mathbf{y}}$ direction at $g = p_0/\rho h$. Incompressibility is assumed,

$$\mathbf{D} \cdot \mathbf{I} = 0. \quad (5)$$

The momentum equation in this frame is

$$\rho \dot{\mathbf{v}} = -\nabla p + \nabla \cdot \mathbf{S} - \rho g \hat{\mathbf{y}}, \quad (6)$$

where p is the isotropic pressure.

The cited authors assume a perturbation with the same spatial distribution as the infinitely thick, inviscid, constant density fluid R-T eigenfunction¹² for their analytic approximations,

$$(v_x, v_y, v_z) = \dot{q} e^{-ky} (\sin kx, \cos kx, 0), \quad (7)$$

but with the time dependent amplitude $q = q(t)$ determined self-consistently from the global balance of kinetic energy, "gravitational" potential energy, and elastic-plastic work. Basing these on the form of Eq. (7) yields,¹⁴

$$\frac{\rho \lambda \dot{q}}{2k} (1 - e^{-2kh}) (\ddot{q} - gkq) + \int_{V^t} \dot{W} = 0. \quad (8)$$

Here, the integral is over one wavelength $\lambda = 2\pi/k$ of the time varying plate volume V^t . We clearly must be able to approximate a section of an imploding shell as being planar for Eq. (7) to be useful. Therefore, λ and q must be small compared to the shell's radius. We will also need to treat λ and h as constant, so the perturbation time scale must be small compared to the implosion time scale. The problem then reduces to the effect of the unperturbed \mathbf{S} due to the plate's lateral convergence on the \dot{W} integral in Eq. (8).

In the rigid-plastic limit (L-M flow), substituting Eq. (7) into Eq. (3), then Eq. (3) into Eq. (2), then Eq. (2) and Eq. (3) into $\dot{W} = \mathbf{S} \cdot \mathbf{D}$, and then substituting that into Eq. (8) results in a nonlinear second order differential equation for q whose solution depends exclusively on the initial values of q and \dot{q} , along with the material constants and dimensions. Perturbation growth in the rigid-plastic limit, then, does not depend on the unperturbed stress field. Miles¹⁵ presents the solution to this equation and derives an initial amplitude condition for stability,

$$|q_0| < \frac{4s_1 h}{(1 + e^{-kh}) p_0}. \quad (9)$$

We will return to this expression by the end of Sec. III, where it will be rederived as the large shear modulus limit of the P-R stability criteria derived in this article.

The P-R flow model may be used to quantify the effects of elasticity and the unperturbed stress deviator due to shell convergence. The $\dot{\mathbf{S}}$ term in Eq. (1) suggests that an integration constant corresponding to the initial value of \mathbf{S} will appear in the solution to $q(t)$. White^{11,14} derives the equivalent of the following from Eq. (8) using an expression for \dot{W} assuming P-R flow,

$$\frac{d^2 \eta}{d\tau^2} = \eta - 4K \frac{e^{KL_A(\eta - \eta_0)} - L_A([\eta - \eta_0]e^{-K})}{\Pi \sinh K},$$

$$L_A(x) \equiv \frac{1}{x} \ln(\cosh x + \sqrt{1 + A \sinh^2 x}). \quad (10)$$

Unitless variables are introduced for a more complete coverage of parameter space in the graphical solution representations which follow. $\eta = 2Gkq/s_1$, with η_0 its initial value, $\tau = \sqrt{gk}t$, $K = kh$, $\Pi = p_0/G$, and A is related to the components of the background (i.e. unperturbed) \mathbf{S} by

$$A = 1 - [(S_{xx} - S_{yy})/2s_1]^2 + (S_{xy}/s_1)^2. \quad (11)$$

The convergence geometry of an exploding or imploding shell can only be defined locally in a planar model in terms of the unperturbed ($q=0$) strain rate tensor \mathbf{D} . \mathbf{S} is simply related to \mathbf{D} in the rigid plastic limit [Eq. (2)]. This limit is usually adequate for describing large strains well beyond the yield limit in metals¹³ such as those found in imploding/exploding shells. Parameter A , then, can be interpreted as parameterizing the effects of convergence geometry on local R-T growth.

TABLE I. Stress parameters for various geometries and modes.

Convergence	Perturbation	(S_{xx}, S_{yy}, S_{zz})	A
cylindrical	azimuthal	$(-1, 1, 0)s_1$	0
spherical	any	$(-1, +2, -1)s_1/\sqrt{3}$	1/4
cylindrical	axial	$(0, 1, -1)s_1$	3/4
flat	any	$(0, 0, 0)$	1

The circumferential component of strain rate for a hoop of radius R collapsing at radial velocity V is simply, from Eq. (3), $-V/R$. If we apply our model to a small section of a sphere uniformly imploding locally in the $+y$ direction, with the x (direction of perturbation periodicity) and z unit vectors being tangential to the surface of the sphere (circumferential), then the *unperturbed* \mathbf{D} components are $D_{xx}=D_{zz}=-V/R$. The trace of \mathbf{D} equals zero due to incompressibility [Eq. (5)], so $(D_{xx}, D_{yy}, D_{zz}) = (-1, +2, -1)V/R$ for an imploding sphere. The rest of the \mathbf{D} components equal zero since we have chosen principal strain axes. For cylindrical implosions, if we assume that the perturbation's periodic x variation is in the axial direction, the z -direction is locally azimuthal (ie. circumferential, so $D_{zz}=-V/R$), the implosion is (again) locally in the y -direction, and the cylinder is confined in the axial direction ($D_{xx}=0$), we have $(D_{xx}, D_{yy}, D_{zz}) = (0, 1, -1)V/R$, with other components zero. Likewise, if the x direction of periodicity is in the azimuthal direction (but keeping the direction of implosion y) $(D_{xx}, D_{yy}, D_{zz}) = (-1, 1, 0)V/R$. From Eq. (2) and the above, Table I summarizes the nonzero components of \mathbf{S} along with A for the above convergence geometries and modes.

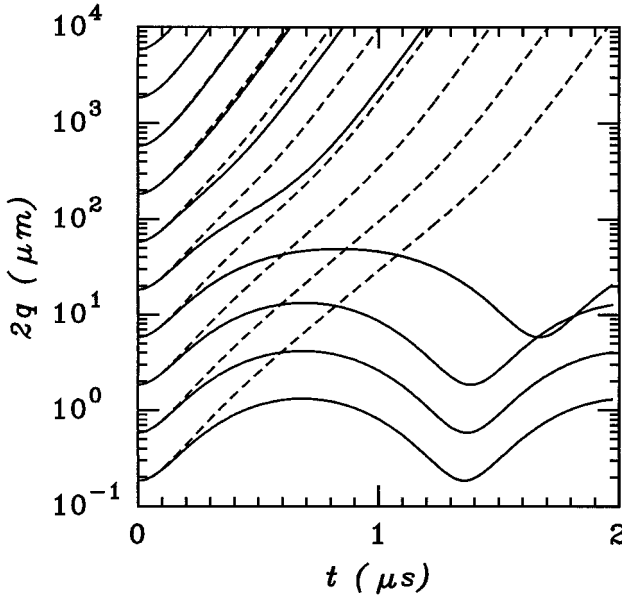


FIG. 2. Perturbation evolution of an accelerated tungsten plate or shell based on Eq. (10) for a range of q_0 values (initial $dq/dt=0$) with $A=1$ (flat plate, solid lines) and $A=0$ (cylindrical flute mode, dashed lines). $h=2.0$ mm, $s_1=11.5$ GPa, $G=94.8$ GPa, $p_0=1200$ GPa, $g=3.11 \times 10^{10}$ m/s², and $k=20.9$ cm⁻¹ ($\lambda/h=1.5$ and $\rho=1.93 \times 10^4$ kg/m³).

Numerical solutions to Eq. (10) are plotted for a range of q_0 values in Fig. 2 for the case of an accelerated tungsten plate. Parameters are chosen to correspond closely to those for which two-dimensional (2D) dynamic hydrocode simulations are available for comparison,^{16,17} as discussed in Sec. IV. The value of G used is calculated from the simulation's input density, sound speed, and Poisson's ratio,¹⁸ and $s_1=Y_0/\sqrt{3}$ is used,¹³ where Y_0 is the simulation's initial yield strength. The same results, but for the maximally converging case of $A=0$, corresponding to the cylindrical azimuthal ("flute") mode, are plotted on the same graph. It is apparent that lateral convergence has a significant adverse impact on the maximum stable initial perturbation amplitude. The $A=0$ case is unstable for an arbitrarily small initial perturbation, as may be verified from the criteria derived in Sec. III.

It is insightful to point out here that Eq. (10) has the form of a classical static potential well since acceleration $d^2\eta/d\tau^2$ depends only on η and time constant parameters. The initial η value η_0 is indeed an unconventional parameter for a well potential but is, nonetheless, constant. Stable perturbations, therefore, result in periodic oscillation within the well, and unstable perturbations occur when there is sufficient "energy" to escape the well without stopping, with η increasing without bound.

Using the identity,

$$\frac{d^2\eta}{d\tau^2} \equiv \frac{1}{2} \frac{d}{d\eta} \left[\frac{d\eta}{d\tau} \right]^2, \quad (12)$$

we derive from Eq. (10),

$$\frac{d\eta}{d\tau} = \pm \left[\left(\frac{d\eta}{d\tau} \right)_{\tau=0}^2 + \eta^2 - \eta_0^2 - 8Ke^K \right. \\ \left. \times \frac{Li_A(\eta - \eta_0) - Li_A([\eta - \eta_0]e^{-K}) - \ln(2)K}{\Pi \sinh K} \right]^{1/2};$$

$$Li_A \equiv \int_1^x L_A dx. \quad (13)$$

The $\ln(2)K$ term results from the requirement that the numerator $\rightarrow 0$ as $\eta \rightarrow \eta_0$. The applications of Eq. (13) are threefold. First, it is used along with Eq. (10) to generate the time power expansion terms in the numerical solutions to $\eta(\tau)$, as described in Appendix B. Second, given a routine for finding $Li_A(x)$ for any x (also discussed in Appendix B), trajectory phase diagrams may be plotted directly. Third, Eq. (13) is used for the derivation of the stability criteria of the model, the subject of Sec. III.

A phase diagram is illustrated in Fig. 3 for the same conditions as Fig. 2. Important features of the trajectory may be illustrated with this representation without the need for the complete numerical solution to the time history such as stability thresholds, the onset amplitude for exponential growth of unstable solutions, and the maximum amplitude of stable solutions. One interesting feature apparent in Fig. 3 is the fact that trajectories with different values of η_0 , but with all else being equal, may cross in phase space. This feature is traceable to the explicit η_0 dependence of the $(\eta, d\eta/dt)$ relationship of Eq. (13). This may be contrasted to corre-

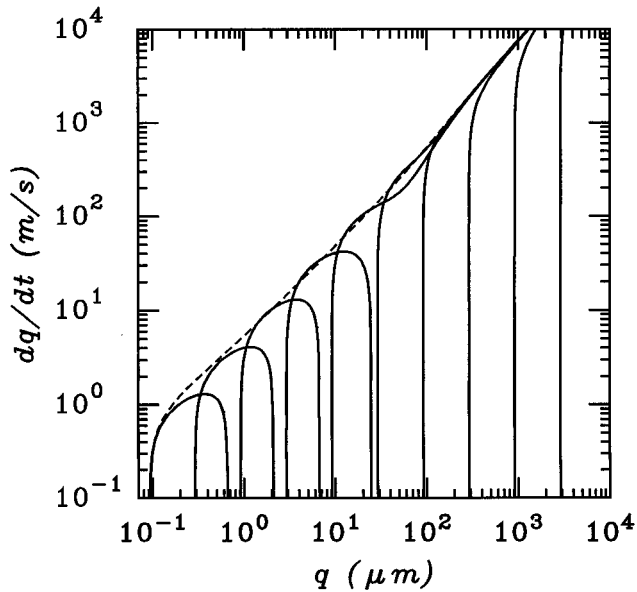


FIG. 3. Phase trajectories for the plots of Fig. 2. $A=1$ (solid lines) and $A=0$ (dashed line). Only the plot with the lowest q_0 is plotted for $A=0$.

sponding phase plots for rigid plastic models.¹⁴ Elastic potential energy constitutes an extra internal degree of freedom for our model which may be different for perturbations with different values of η_0 (the amplitude at which the elastic energy is zero), even at the point in their respective evolutions when they have the same η and $d\eta/dt$ values.

III. STABILITY CRITERIA

The term in large square brackets in Eq. (13) may be interpreted as the negative of the well's effective "potential." The maximum amplitude $\eta = \eta_m$ of a *stable* solution will occur at the turn-around point when this term, and therefore $d\eta/d\tau$, are equal to zero. Unstable solutions will have the distinguishing property of having no real solution to $d\eta/d\tau=0$ for $\eta > \eta_0$. To avoid muddling the math with a term usually not used anyway, we henceforth confine ourselves to the case $(d\eta/d\tau)_{\tau=0} = 0$, although it may be easily added by the reader. Introducing the new variables $\eta_{\pm} = (\eta_m \pm \eta_0)$ (with inverse relationships $\eta_m = (\eta_+ + \eta_-)/2$, $\eta_0 = (\eta_+ - \eta_-)/2$) permits separation of variables for our $\eta = \eta_m$ condition. Solving the rhs of Eq. (13) for zero, we get,

$$\Pi \eta_+ = 8Ke^K \frac{Li_A(\eta_-) - Li_A(\eta_- e^{-K}) - \ln(2)K}{\eta_- \sinh K}. \quad (14)$$

The change of variables $(\eta_m, \eta_0) \rightarrow (\eta_-, \eta_+)$ is an axis rotation in parameter space by an angle of $\frac{1}{4}\pi$ followed by an amplification of $\sqrt{2}$.

Figures 4 and 5 plot $\Pi \eta_+$ vs η_- for a range of K values for the extreme cases of $A=1$ and $A=0$, respectively. Together, these plots fully represent the dimensionality, if not the range, of parameter space (though only coarsely for parameter A). To determine η_m for any given Π , overlay the η_0 and η_m axes on these plots and read off η_m for a given η_0 (and K). The new axes will generally be skewed in ad-

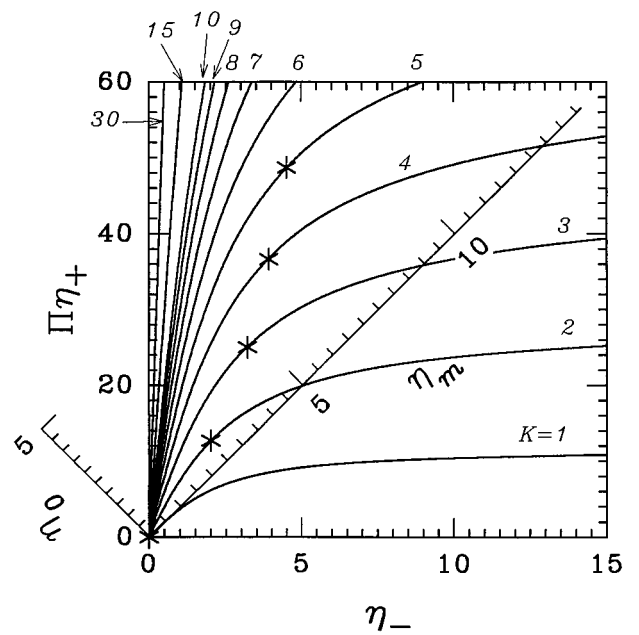


FIG. 4. $\Pi \eta_+$ vs η_- for a range of K for $A=1$ (flat plate). The (η_m, η_0) axes corresponding to the $\Pi=4$ case are overlaid. $\eta_0 = \eta_c$ for $\Pi=4$ is marked with (*) on each curve. Note that $\eta_c \rightarrow 0$ as $K \rightarrow 1$.

dition to being rotated and rescaled because η_+ is multiplied by Π in the plots so that parameter space may be better spanned. The sample axes overlays on the figures, however, are conveniently chosen to correspond to $\Pi=4$, for which equal η_+ and η_- increments correspond to equal distances on the graph. The rotated axes, therefore, are orthogonal. One finds that for any given positive η_0 , there are often two solutions to η_m . The larger solution corresponds to a point of equal effective potential outside the well (the potential

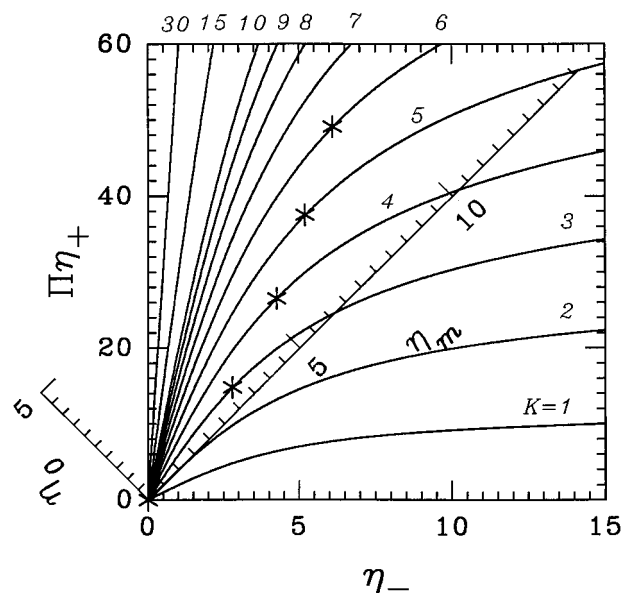


FIG. 5. Same plot as Fig. 4, except for $A=0$ (cylindrical flute mode). Note that $\eta_c \rightarrow 0$ as $K \rightarrow 2$.

falls off again), and is therefore dynamically inaccessible to the stable (bound) solution that the function represents.

For our first stability threshold criterion, We seek η_c [q_c], defined as the maximum η_0 [q_0] which results in a stable solution. Consider the function $\eta_0(\eta_m)$, defined as the $-\frac{1}{4}\pi$ rotation and $\sqrt{2}$ attenuation of $\eta_+(\eta_-)$ based on Eq. (14). A candidate for η_c is η_0 where $d\eta_0(\eta_m)/d\eta_m=0$ (a local extremum). These extrema for $\Pi=4$ for each K are

$$\Pi = 8Ke^K \frac{sL_A(s) - se^{-K}L_A(se^{-K}) - Li_A(s) + Li_A(se^{-K}) + \ln(2)K}{s^2 \sinh K}. \quad (15)$$

Plugging this into Eq. (14), solving for the extremum $r = \eta_+$, and rotating back to the (η_m, η_0) frame ($\eta_c = (r - s)/2$) results in

$$\eta_c = \frac{s}{2} \frac{2Li_A(s) - 2Li_A(se^{-K}) - 2\ln(2)K - sL_A(s) + se^{-K}L_A(se^{-K})}{sL_A(s) - se^{-K}L_A(se^{-K}) - Li_A(s) + Li_A(se^{-K}) + \ln(2)K}. \quad (16)$$

Equation (15) together with Eq. (16) provide the relationship η_c vs Π via intermediate parameter s , and may be plotted directly by calculating both for a range of s values. Figures 6 and 7 illustrate such plots for $A=1$ and $A=0$, respectively, in a form useful for general reference.

It is apparent from Fig. 6 and Fig. 7 that $\eta_c \rightarrow 0$ at some finite Π . For the case of $\Pi=4$, $\eta_c \rightarrow 0$ is illustrated as the $K=1$ and $K=2$ extrema (“*”) plotted in Figs. 4 and 5, respectively. η_c decreases and Π increases as s decreases. $\eta_c \rightarrow 0$ and $\Pi \rightarrow 2K(1+A)$ as $s \rightarrow 0$. The derivatives needed

shown as “*” in Figs. 4 and 5. It is clear from the parameter spanning solutions plotted here that this is, in fact, η_c . A rigorous proof that this local extremum is the global maximum could be accomplished by proving that $d\eta_0^2(\eta_m)/d\eta_m^2 < 0$ everywhere (as is apparently the case), but is not attempted. In the (η_-, η_+) frame, this condition is $d\eta_+(\eta_-)/d\eta_- = 1$. Applying this condition to Eq. (14) and defining $s = \eta_-$ at the extremum, we get

to use L’Hôpital’s rule to verify these limits may be derived with the help of the small x approximation from Eq. (B1). This limiting value of Π , defined as Π_c , identifies the driver pressure p_0 threshold $p_c = G\Pi_c$ beyond which infinitesimal perturbations are unstable,

$$p_c = 2Gkh(1+A). \quad (17)$$

Π_c in Figs. 6 and 7 is the abscissal value of the plots as the ordinate, and therefore η_c , goes to zero. The large η_c asymptotes, on the other hand, correspond to the large G , or rigid plastic, limit. Noting that η_c increases as s increases, we may rederive the stability criterion [Eq. (9)] in the rigid

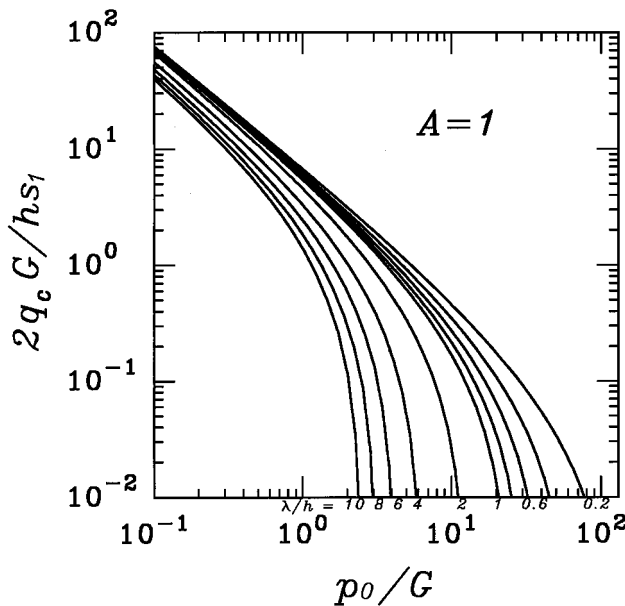


FIG. 6. Rayleigh–Taylor stability diagram η_c/K vs Π for a range of $2\pi/K$ values for $A=1$, corresponding to an elastic-plastic flat plate. The axes, here, are labeled in terms of variables with conventional units: q_c is the critical initial amplitude beyond which instability occurs, p_0 is the driver pressure, G is the elastic shear modulus, h is the plate thickness, s_1 is the von Mises yield strength in pure shear, and λ is the perturbation wavelength.

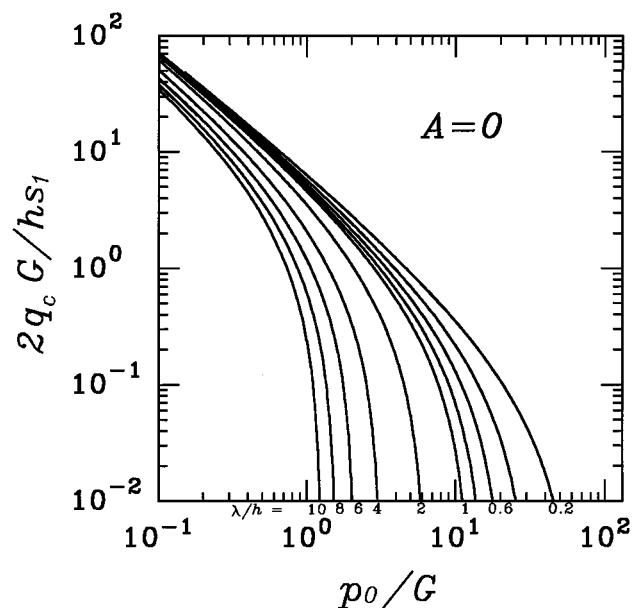


FIG. 7. η_c/K vs Π for $A=0$, corresponding to the flute mode of a cylindrical implosion or explosion. Lateral material convergence, as parameterized by A [Eq. (11)], has its greatest destabilizing effect for this geometry and mode.

plastic limit by multiplying Eq. (15) by Eq. (16) and taking the limit of $s \rightarrow \infty$. The limiting forms $L_A(s) \rightarrow 1$ and $Li_A(s) \rightarrow s$ for large s , based on Eq. (B1), are adequate for this procedure. Reverting to conventional variables and solving for q_c , we obtain

$$q_c \rightarrow \frac{4s_1 h}{(1 + e^{-kh})p_0} \quad \text{as } G \rightarrow \infty. \quad (18)$$

This is equivalent to Eq. (9).

IV. DISCUSSION

Robinson and Swegle,¹⁴ with only solutions to the equation of motion to work with, coarsely mark the domain of instability of a formally related R-T model (EPII) in $(q_0, \lambda/h)$ parameter space for the special case of aluminum with $G=15$ GPa, $s_1 = Y/\sqrt{3} = 0.19$ GPa, and $h=2.54$ cm using three different values of p_0 in their Fig. 9. Figure 9 provides a convenient spot check for our own Fig. 6. For example, their lowest “×” mark for $\lambda/h=2$ implies that with $p_0=60$ GPa, the transition to instability occurs for q_0 somewhere between 10 and 20 μm . This corresponds to $\Pi=4$ and a value of η_c/K between 0.06 and 0.12. The actual value of our $\lambda/h=2$ curve in Fig. 6 at $\Pi=4$ is $\eta_c/K=0.16$ (reasonable agreement).

In related work,^{16,17} the above authors present results of the 2D dynamic simulation of a tungsten plate from which the parameters of Fig. 2 are based. The simulation assumes, though, that the driver pressure is ramped up to 1200 GPa over the first 2.5 μs . Figure 2 agrees fairly well with the stable cases’ oscillation amplitude and period, and the stability threshold value $q_0 = q_c$, but only if one takes the *effective* q_0 in the simulation to be q at the end of the ramp phase. The actual q_0 is two orders of magnitude less. This emphasizes the primacy of the constant acceleration assumption of Eq. (10).

Equation (17) is the critical pressure p_c for stability of an infinitesimal initial perturbation based on the general (large amplitude) equation of motion [Eq. (10)]. The same value of p_c does in fact result from Robinson and Swegle’s¹⁴ Eq. (48) (small amplitude approximation). This equation implies that small amplitude, marginally stable solutions oscillate with a peak amplitude of the same order as the initial perturbation, and is therefore adequate for describing the stability of initially infinitesimal perturbations for more general equation of motion. Equation (17) is a simple but important result since it concisely quantifies a fundamental limit on how hard plates and shells can *theoretically* be accelerated over significant distances. It explains infinitesimal perturbation stability thresholds observed in dynamic solutions¹⁴ to Eq. (10), and in the aforementioned numerical tungsten simulations as well.^{16,17} Plots of stability boundaries in (q_0, K) parameter space for a range of yield strengths for variants of the tungsten simulation¹⁷ (with all other parameters unchanged) show that the critical pressure for $K=2.79$ and $G=94.8$ GPa is 1200 GPa with, as is the case with Eq. (17), little sensitivity to yield strength. From Eq. (17), with $A=1$, $p_c=1057$ GPa. So, despite the q_0 discrepancy, p_c is similar in the tungsten simulation to that defined

by Eq. (17). This is consistent with the general agreement of our analytic model *after* the pressure ramp (at least in the case discussed), and the fact that an infinitesimal perturbation after enhanced (but finite) amplification during the pressure ramp is still infinitesimal.

The lack of an s_1 dependence in Eq. (17) is traceable to the fact that s_1 appears only in the denominator of the normalization factor between q [q_c] and η [η_c]. s_1 , therefore, has an inverse proportionate effect on the magnitude of q_c , all else being equal, but no effect on whether perturbations with infinitesimal values of q_0 are stable. Though an approximation, this independence implies at least that p_c is insensitive to s_1 in exact P-R flow. Also, since stable solutions are periodic, the details of energy dissipation appear to be relatively unimportant for describing their dynamics. This suggests a general insensitivity to the flow *model* of the inelastic regime up to the point of instability (at least for $A=1$, where there is no background plastic flow). Equation (17) should therefore provide a useful reference pressure for accelerated plates made of any material with an isotropic shear modulus, even if P-R flow is inapplicable (e.g., ceramics, quartz).

The finite value of q_c , however, is of interest for the purpose of establishing surface finish tolerances for cases where the driver pressure falls below p_c . In such cases, Fig. 6, Fig. 7, or the corresponding plot calculated for the particular value of A involved, should be referred to. We see from these figures that sufficiently large initial perturbations will grow unstably for driver pressures an order of magnitude below p_c before the rigid plastic limit (the left asymptotes of the curves) becomes accurate. Furthermore, we see from the following example that such sufficiently large perturbations may, nonetheless, be sufficiently small to be of concern in regard to realistic machining tolerances.

As an empirical check of the usefulness of the model for a converging geometry, a confirmation that the instability observed in Fig. 1 is consistent with the initial 130 μm machining error is here performed. This error was measured with a micrometer before the implosion and has a characteristic scale length of a few cm. It is apparent from the radiographic data that an outer perturbation with a wavelength-shell thickness ratio of $\lambda/h \sim 2$ at 14 μs grows during the implosion. Plots from the CALE simulation of S_{zz} , S_{rr} (cylindrical coordinates), and s_1 at this time reveal that $A \approx 0.26$ in the bulk of the equatorial region at 14 μs , based on Eq. (11) ($z \rightarrow x$ and $r \rightarrow y$). This is quite close to the theoretical value of $A=1/4$ for a sphere, despite the fact that the liner shown in Fig. 1 departs significantly from a sphere at this time. The initial perturbation amplitude-shell thickness ratio is $q_0/h \approx 0.13$. The applied driver pressure is $p_0 \sim 10$ GPa. According to the CALE results, the time dependent values of G and s_1 are still within 40% of their initial values at 14 μs . So, within reasonable accuracy, we may use the 6061-T6 Al initial values^{7,8} $G=28$ GPa and $s_1 = Y/\sqrt{3} = 0.17$ GPa (Y is the uniaxial yield strength) for our analytic model. These numbers give $\Pi=0.35$ and $\eta_0/K=42.8$. However, the stability threshold for η_0/K is only $\eta_c/K=15.6$ at $\Pi=0.35$ for $\lambda/h=2$, as read from a plot similar to Figs. 7 and 8, but for $A=1/4$. The mode is there-

fore theoretically unstable for the actual machine tolerances used.

It is interesting to note that, from Eq. (17), $p_c = 219$ GPa for the above example. This, being an order of magnitude above the actual applied pressure, indicates that, given improvements in machining tolerances, stable implosions should result even if significantly higher pressures are applied. Although we abuse the limits of the approximations made in our simplified model, the example serves to illustrate the usefulness of the model for determining permissible machining tolerances, establishing the feasibility of scaling experiments to higher energies, and in narrowing parameter searches for more detailed simulations of the R-T instability in solids. To better establish the degree of usefulness of the model, however, simulations with imposed initial perturbations with η_0/K above and below $\eta_c/K = 15.6$ should be performed. Likewise, the significance of parameter A should be checked by performing simulations in planar and converging geometries using values of η_0/K that are predicted by the model to be stable in planar geometry, but unstable in converging geometry due to the decrease in the value of A .

ACKNOWLEDGMENTS

One of the authors, (E.L.R.) wishes to acknowledge the help of S.E. Englert and A.L. Chesley for help in the image analysis used in the preparation of Fig. 1. The source code and associated technical documentation for FORTRAN function LI, which calculates $Li_A(x)$, is available upon request to E.L.R.

APPENDIX A: MAGNETIC DRIVERS

In many applications, such as the quasispherical solid shell implosions discussed in Secs. I and IV, one has a conducting solid driven by a magnetic "fluid," where the magnetic field diffusion is significant, instead of a massless gas driver assumed in the R-T model of interest. We consider here the conditional applicability of this model to a plate of finite but otherwise arbitrary electrical conductivity accelerated by magnetic pressure. The momentum equation [Eq. (6)] in this case must be generalized to include the effects of the magnetic field \mathbf{B} ,¹⁹

$$\rho \dot{\mathbf{v}} = -\nabla(p_{mat} + p_{mag}) + \frac{(\mathbf{B} \cdot \nabla)\mathbf{B}}{\mu_0} + \nabla \cdot \mathbf{S} - \rho g \hat{\mathbf{y}}, \quad (\text{A1})$$

where p_{mat} and $p_{mag} \equiv B^2/2\mu_0$ are the isotropic material and magnetic pressures, respectively. \mathbf{B} itself satisfies the magnetic diffusion equation,¹⁹

$$\frac{\partial \mathbf{B}}{\partial t} = \nabla \times (\mathbf{v} \times \mathbf{B}) + \frac{1}{\mu_0 \sigma} \nabla^2 \mathbf{B}, \quad (\text{A2})$$

where σ is electrical conductivity.

The first condition for applicability is clearly that $(\mathbf{B} \cdot \nabla)\mathbf{B} = 0$ in Eq. (A1). This is satisfied in planar geometry (the limit of radius $r \gg h$ for shells of thickness h) if we constrain ourselves to a magnetic field of the form $\mathbf{B} = B(x, y)\hat{\mathbf{z}}$ resulting from a constant current per unit length in the z direction I which closes its circuit on the side that the plate is accelerating away from. To be consistent with

this, only z invariant (two dimensional) perturbations are considered. Eq. (A1) is then equivalent to Eq. (6) provided we define $p \equiv p_{mat} + p_{mag}$. This definition has no effect on Eq. (5), fortunately, since there is no independent p_{mat} dependence in this equation of state, as there would be for a compressible medium. Dynamical equivalence is then implied if the boundary conditions are equivalent. Fortunately, Ampere's law implies that, regardless of the detailed form of \mathbf{B} in the interior resulting from diffusion, $\mathbf{B} = \mu_0 I \hat{\mathbf{z}}$ (constant) on the lower surface. The boundary condition there is then equivalent to the gas driver case with $p = p_0 = \frac{1}{2}\mu_0 I^2$ there. Voids (bubbles) and breaks in the plate must explicitly be assumed to be absent to avoid the resultant complications in the boundary conditions. Given the above constraints, then, the dynamics of a magnetically driven plate is equivalent to the gas driver case. The addition of Eq. (A2) serves only to determine the relative contribution of p_{mag} to p at any given point and time.

The above proof of conditional equivalence is worth further discussion since there is a certain counterintuitiveness to it which has led to considerable controversy. Intuitively, one might think that a redistribution of the internal magnetic pressure due to diffusion (a dissipative effect) would have an effect on the dynamics of, say, R-T spikes or streamers thinner than the magnetic skin depth (the proof makes no linear approximation). But, as implied above, any local increase in p_{mag} due to diffusion is exactly offset by a corresponding decrease in p_{mat} relative to what it would be in the gas driver case. This holds as long as the external coupled circuit is able to supply enough energy to offset Ohmic dissipation so as to maintain a constant current I . This equivalence is clearly traceable to the assumption that the relative drop in p_{mat} has no effect on local density. Compressibility would have introduced an equation of state involving p_{mat} independent of p_{mag} , thereby requiring the coupling of the magnetic diffusion equation for p_{mag} for mathematical closure.²⁰ In contrast, when significant compressibility of a magnetically accelerated medium is present (as for a plasma), magnetic diffusion has a significant effect on the dynamics, dissipating the streamers which appear in the nonlinear phase of the R-T instability by allowing them to broaden and merge.²¹

For magnetically driven shells, due to the $(\mathbf{B} \cdot \nabla)\mathbf{B} = 0$ requirement, our model describes axial wave numbered modes in the $r \gg h$ limit for azimuthal magnetic drivers (z pinches), and azimuthal modes for axial magnetic drivers (θ pinches). Modes parallel to the magnetic field are stable, as they are for a perfect fluid.

APPENDIX B: NOTES ON NUMERICAL SOLUTIONS

Coding a general routine for calculating $Li_A(x)$ for any $x > 0$ is a useful first step in numerically evaluating the results of Sec. III. Supplementing a purely numerical integration derived lookup table for $Li_A(x)$ in the region $(0.1 \leq x \leq 10)$ with contributions based on the limiting forms,

$$L_A(x) \approx \begin{cases} \ln(2)x^{-1} + (1+A)x/4 + (1-2A-9A^2)x^3/96 & \text{if } x < 0.1; \\ 1 + \ln[(1 + \sqrt{A})/2]x^{-1} & \text{if } x > 10, \end{cases} \quad (\text{B1})$$

which have simple analytic integrals, minimizes problems associated the divergence of $L_A(x)$ as $x \rightarrow 0$, and simplifies integration for large x . These approximations are based on the Taylor series expansion of $xL_A(x)$ for small x , and the asymptotic forms of cosh and sinh for large x . They are accurate to within a factor of 10^{-8} in their respective regions.

Equations (10) and (13) are used for our numerical solutions to η vs τ presented in Sec. II. Given these first two τ derivatives of η , as functions of η itself [Eqs. (10) and (13)], one may derive any higher derivative desired by consecutive η differentiation and application of the chain rule. These terms may then be used to iteratively calculate η vs τ by N th order polynomial extrapolation across discrete τ intervals,

$$\eta_{i+1} = \eta_i + \sum_{n=0}^N \left(\frac{d^n \eta}{d\tau^n} \right)_i \frac{(\tau_{i+1} - \tau_i)^n}{n!}, \quad (\text{B2})$$

where subscript i means solve at the start of the i th τ interval. For $\tau_0=0$, the $\eta \rightarrow \eta_0$ limit must be taken for the η derivatives. For Eq. (10), for example, this gives $(d^2 \eta/d\tau^2)_0 = \eta_0$. Any change in the sign of $d\eta/d\tau$, which is left undetermined in Eq. (13), may be determined from a sign change in $(d\eta/d\tau)_{i+1}$, as calculated from the τ derivative of the i th extrapolation polynomial.

¹J. Barnes, P. Blewett, R. McQueen, K. Meyer, and D. Venable, *J. Appl. Phys.* **45**, 727 (1974).

²J. Barnes, D. Janney, R. London, K. Meyer, and D. Sharp, *J. Appl. Phys.* **51**, 4678 (1980).

³J. Degnan, M. Alme, W. Baker, J. Buff, C. Boyer, C. Clouse, S. Coffey,

D. Conley, D. Dietz, J. Graham, S. Gonzalez, K. Hackett, D. Hall, J. Holmes, E. Lopez, W. McCullough, D. Price, R. Reinovsky, N. Roderick, P. Turchi, and J. Welby, *Megagauss Technology and Pulsed Power Applications, Fourth International Conference on Megagauss Magnetic Field Generation and Related Topics*, edited by C. Fowler, R. Caird, and D. Erickson (Plenum, New York, 1987), pp. 609–706.

⁴J. Degnan, W. Baker, M. Alme, C. Boyer, J. Buff, J. Beason, C. Clouse, S. Coffey, D. Dietz, J. Frese, J. Graham, D. Hall, E. Holmes, J. L. Lopez, R. Peterkin, D. Price, N. Roderick, S. Seiler, and P. Turchi, *Fusion Tech.* **27**, 115 (1995).

⁵J. Degnan, W. Baker, J. Beason, C. Clouse, D. Dietz, D. Hall, J. Holmes, D. Price, C. Sovinec, J. Graham, E. Lopez, M. Alme, S. Coffey, S. Seiler, P. Turchi, J. Buff, M. Frese, R. Peterkin Jr., and N. Roderick, *Megagauss Fields and Pulsed Power Systems, Fifth International Conference on Megagauss Magnetic Field Generation and Related Topics*, edited by V. Titov and G. Shvetsov (Nova Science, New York, 1990), pp. 623–630.

⁶J. Degnan, F. Lehr, J. Beason, G. Baca, D. Bell, A. Chesley, S. Coffey, D. Dietz, D. Dunlap, S. Englert, D. Gale, J. Graham, C. Haveranek, J. J. Holmberg, T. Hussey, R. Lewis, C. Outten, R. Peterkin, Jr., D. Price, N. Roderick, E. Ruden, U. Shumlak, G. Smith, and P. Turchi, *Phys. Rev. Lett.* **74**, 98 (1995).

⁷D. Steinberg, S. Cochran, and M. Guinan, *J. Appl. Phys.* **51**, 1498 (1980).

⁸D. Steinberg, Technical Report No. UCRL-MA-106439, Lawrence Livermore National Laboratory, 1996.

⁹R. Tipton, *A 2D Lagrange MHD Code*, in Fowler *et al.* (Ref. 3) p. 299.

¹⁰R. Tipton, *CAL Users Manual* (Lawrence Livermore National Laboratory, Livermore, CA, 1991).

¹¹G. White, Technical Report No. LA-5225-MS, Los Alamos Scientific Laboratory, 1973.

¹²S. Chandrasekhar, *Hydrodynamic and Hydromagnetic Stability* (Dover, New York, 1961).

¹³A. Kahn and S. Huang, *Continuum Theory of Plasticity* (Wiley, New York, 1995).

¹⁴A. Robinson and J. Swegle, *J. Appl. Phys.* **66**, 2859 (1989).

¹⁵J. Miles, Technical Report No. GAMD-7335, General Dynamics, 1966.

¹⁶A. Robinson and J. Swegle, Technical Report No. SAND87-0766, Sandia National Laboratory, 1987.

¹⁷J. Swegle and A. Robinson, *J. Appl. Phys.* **66**, 2838 (1989).

¹⁸L. Landau and E. Lifshitz, *Theory of Elasticity*, 2nd ed. (Pergamon, New York, 1970).

¹⁹G. Schmidt, *Physics of High Temperature Plasmas*, 2nd ed. (Academic, New York, 1979).

²⁰R. Hazeltan and J. Meiss, *Plasma Confinement* (Addison-Wesley, Redwood, CA, 1992).

²¹N. Roderick and T. Hussey, *J. Appl. Phys.* **56**, 1387 (1984).

²²D. Drucker, *Mech. Today* **5**, 37 (1980).